

# International Conference on Space Optics—ICSO 2022

Dubrovnik, Croatia

3–7 October 2022

*Edited by Kyriaki Minoglou, Nikos Karafolas, and Bruno Cugny,*



## *Enhanced Resolution Light Scattering Analyzer for Curved Gratings – ELSA/CG-S*



# Enhanced Resolution Light Scattering Analyzer for Curved Gratings – ELSA/CG-S

Matthias Zilk<sup>\*</sup>, Tilman Glaser<sup>1</sup>, Felix Koch<sup>1</sup>, Martin Steglich<sup>1</sup>, Thomas Wollweber<sup>1</sup>, Dennis Lehr<sup>1</sup>,  
Dana Tomuta<sup>2</sup>, Mathijs Arts<sup>2</sup>, Volker Kirschner<sup>2</sup>

<sup>1</sup>Carl Zeiss Jena GmbH, Carl-Zeiss-Promenade 10, 07745 Jena, Germany

<sup>2</sup>ESA/ESTEC, Postbus 299, 2201AG Noordwijk, The Netherlands

<sup>\*</sup>[matthias.zilk@zeiss.com](mailto:matthias.zilk@zeiss.com), +49 3641 64 1654

## ABSTRACT

The knowledge of the bi-directional scattering distribution function (BSDF) of an optical component is an import requirement for the design and assessment of high-performance optical instruments. However, precise BSDF measurement with high resolution close to the specular beam can be very challenging and require sophisticated instrumentation.

In this paper, we present a newly developed scatterometer, the “Enhanced Resolution Light Scattering Analyzer for Curved Gratings (single detector axis)” – ELSA/CG-S which is designed specifically to measure the BSDF of curved optical components with a very high resolution not only close to the specular direction, but throughout the whole angular measurement range with an instrument signature that can compete with the top of the class of current commercially available instruments. The distinguishing feature of the instrument is the use of a high-resolution silicon sCMOS imaging detector which enables fast acquisition times and provides access to a two-dimensional section of the BSDF around the main detection plane of the instrument with an out-of-plane FoV of about  $\pm 0.6^\circ$ .

In the following, we will describe the general design of the instrument and explain the measures that have been taken to enable a very low stray light signature with the chosen detection scheme. After this, we will assess the instruments capabilities and present measurements of the instrument signature and BRDF measurements of plane and curved diffraction gratings with high groove densities. These measurements will also demonstrate the additional value that is provided by using an imaging detector. All measurements will be compared to results obtained with ESTEC’s commercial CASI scatterometer from The Scatter Works, that represent the current state of the art.

**Keywords:** optical scattering, scatterometry, stray light assessment, BRDF measurement, optical testing

## 1 INTRODUCTION

Achieving a good contrast and a high signal to noise ratio is a key requirement for many optical instruments both for spaceborne and terrestrial applications, ranging from spectrometry to high resolution lithography. Achieving this goal relies on a thorough stray light assessment and management which in turn requires a precise knowledge of the bi-directional scattering distribution function (BSDF) of the instrument’s components for modelling and qualification purposes. Measuring the BSDF of optical components can be a very challenging task and requires experience and proper instrumentation [1,2].

The BSDF is a generalization of the hemispherical bi-directional reflectance distribution function (BRDF) which was first introduced by Nicodemus [3]. It is defined as the differential ratio between the radiance scattered into a direction  $(\theta_s, \varphi_s)$  and the irradiance incident from the direction  $(\theta_i, \varphi_i)$  [4]:

$$\text{BSDF} = \frac{dL_s(\theta_s, \varphi_s)}{dE_i(\theta_i, \varphi_i)} \quad (1)$$

For measurement purposes, this can be approximated by

$$\text{BSDF} \approx \frac{\Delta P_s(\theta_s, \varphi_s)}{P_i \Delta \Omega \cos \theta_s} \quad (2)$$

where  $\Delta P_s$  is the Power that is detected by a small detector positioned along the direction  $(\theta_s, \varphi_s)$  covering the solid angle  $\Delta \Omega$  when the surface is illuminated with the incident power  $P_i$ .

Unfortunately, the BSDF is a high-dimensional function. In addition to the directions of the incident and the scattered light, the BSDF also depends on the wavelength and the position on the surface. Thus, it is practically impossible to measure the complete BSDF of a surface. Instead, usually only samples of the BSDF at discrete wavelengths and surface positions are obtained for a finite set of incidence directions. Even then it remains challenging to measure the remaining two-dimensional function  $\text{BSDF}(\vec{r}, \lambda, \theta_i, \varphi_i; \theta_s, \varphi_s) = f(\theta_s, \varphi_s)$  and a further tradeoff between measurement time, resolution, and coverage must be found.

Current commercially available instruments, e.g. CASI from The Scatter Works [5] or Albatross-TT from the Fraunhofer IOF [6], employ a single channel detector with a variable aperture for a pointwise sampling of  $f(\theta_s, \varphi_s)$ . This is quite slow and complicates the detection and characterization of localized BSDF features: Either some extrinsic information about expected BSDF features has to be available to choose suitable aperture settings before a measurement or multiple measurements with different aperture settings have to be made. Albatross-TT has a detector coverage of a full hemisphere, enabling a true 2D measurement. However, the system trades some small angle resolution for a compact design. CASI limits the detector movement to the horizontal plane and avoids any additional optical elements between illumination mirror and detector aperture. This allows for an exceptionally good instrument signature that is only limited by the quality of the illumination mirror. The downside of this approach is that out-of-plane scattering can only be accessed by changing the sample orientation and illumination conditions [1], which might result in a deviation from the application geometry. Comparative measurements between CASI and Albatross-TT can be found in [2].

In our opinion, the single channel approach is a major limitation of these instruments, and much value could be gained in terms of speed, information density and even ease of use, by employing an imaging detector. Due to the technological advances of the last decades, sensitive sCMOS cameras with high resolution and high dynamic range are now available at a reasonable price, and modern desktop computer systems can handle the amounts of data produced by these cameras with ease. We therefore don't see a fundamental reason why a camera based scatterometer should not be able to match the performance of the existing commercial single channel instruments.

The feasibility of using an imaging detector for optical scatter measurements has already been demonstrated by Zeiss with a Czerny-Turner-like scatterometer for plane gratings [7]. Now we extend this concept to a CASI-like design to enable the measurement of a wider range of sample geometries. Of course, adhering to the CASI geometry means that only a small region of the 2D BSDF close to the main detector plane is accessible. However, we think that the potential gain of resolution at arbitrary in-plane scatter angles, the avoidance of the need to choose any detector aperture settings before the measurement, the additional context provided by the out-of-plane FoV, and the access to high resolution spot images for alignment is still very valuable. Also, a later extension to larger out-of-plane angles should be possible with manageable effort by adding another motorized stage to the instrument's detector arm.

## 2 INSTRUMENT DESIGN

### 2.1 Optical and Mechanical Design

The ELSA/CG-S scatterometer that we developed follows the basic design of the CASI scatterometer: The sample is mounted on a central rotation stage that allows adjusting the angle of incidence. The detector is mounted on the cantilever of a second rotation stage that is coaxial to the sample rotation stage. This allows scanning the detector 360° around the sample in the horizontal plane. The schematic beam path of the ELSA/CG-S scatterometer is shown in Figure 1. A comparison of the main system parameters between ELSA/CG-S and CASI is given Table 1. CAD views of the actual instrument are shown in Figure 2.

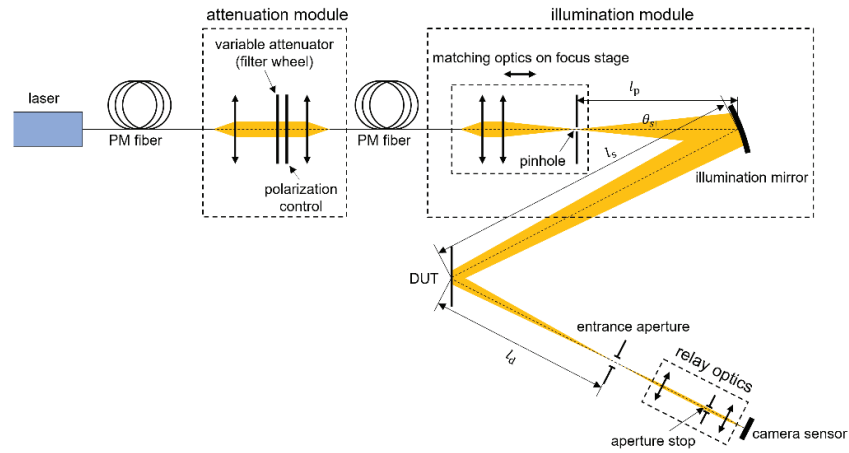


Figure 1: Schematic beam path of the ELSA/CG-S scatterometer.

The scatterometer consists of a main module which houses the actual instrument inside a light-tight enclosure and an electronics cabinet that contains the control PC, power supplies, controllers, and a safety PLC. The footprint of the main module is 2400 mm by 1300 mm which is comparable to the footprint of a small optical table and slightly smaller than the footprint of the CASI scatterometer. The main instrument consists of several modules that are mounted on a common breadboard: A laser, an attenuation module, an illumination module, an axes assembly and a detector module with entrance aperture, relay optics and camera.

Table 1: Comparison of the system parameters between ELSA/CG-S and CASI.

	ELSA/CG-S	CASI
Illumination mirror focal length $f$	320 mm	300 mm
Pinhole to mirror distance $l_p$	315 mm ... 455 mm	ca. 350 mm (signature)
Mirror to sample distance $l_s$	1300 mm	1500 mm
Nominal detector distance $l_d$	350 mm (fixed)	480 mm (adjustable)
Laser wavelength used for measurement	632.69 nm (diode laser with VBG)	632.8 nm (HeNe laser)
Smallest aperture	17.1 $\mu\text{m}$ (pixel size), corresponds to 0.0028° at $l_d = 350$ mm	278 $\mu\text{m}$ , corresponds to 0.0332° at $l_d = 480$ mm
Largest aperture	7.5 mm (entrance aperture size), corresponds to 1.23° at $l_d = 350$ mm	13.8 mm, corresponds to 1.65° at $l_d = 480$ mm
Detector occlusion region	$\pm 6^\circ$	$\pm 4^\circ$
Typical scan file size (-15°...15°)	ca. 250 MB	ca. 25 kB

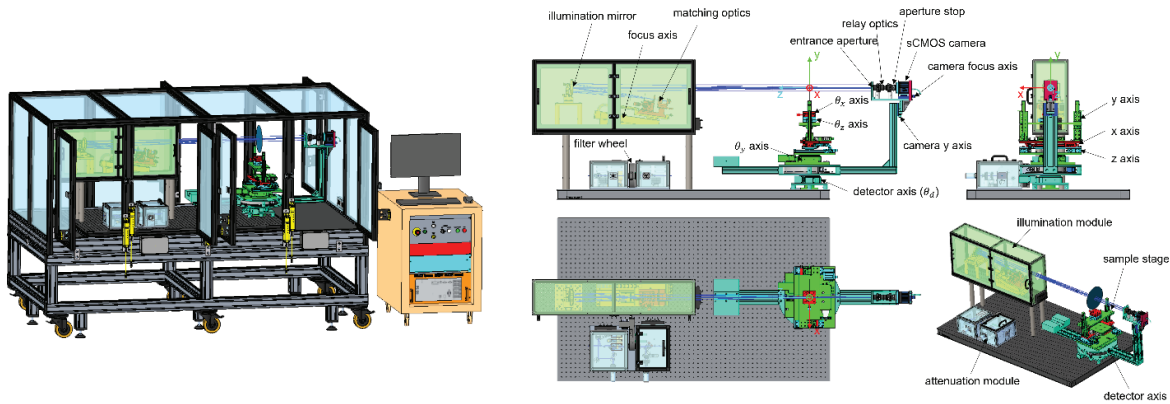


Figure 2: CAD views of the ELSA/CG-S scatterometer and its main components. All transparent enclosure parts are made of black anodized aluminium on the real instrument. The coloring is for illustrative purposes only and does not correspond to the real colors of the components, which are mostly black.

Inside the attenuation module, the output from the laser fiber is collimated and sent through an exchangeable neutral density filter mounted in a motorized filter wheel. Behind the filter wheel, the polarization of the beam can be adjusted by a half wave plate and a linear polarizer before it is coupled into another PM fiber that connects the attenuation module to the illumination module. The attenuation module also contains a laser line filter for background suppression and an optical isolator. The attenuation module allows the adjustment of the laser power in the range from -70 dB to 0 dB in steps of 10 dB. The choice for a filter wheel with discrete filters was made because of the good repeatability, the wide range of available attenuation values, and the fast change times (ca. 57 ms between adjacent filters), which this solution provides.

Inside the illumination module, the fiber is connected to a matching optics which reduces the beam divergence from the fiber by collimating and refocusing the fiber output onto a pinhole which acts as a point source for sample illumination. The light from the pinhole is reflected by the concave illumination mirror with a radius of curvature of 640 mm and is directed to the device under test (DUT) which is at a distance of  $l_s = 1300$  mm from the mirror vertex. The illumination mirror is the heart of the instrument, and its properties largely determine the instruments signature. The mirror has been polished at Zeiss to a very high fidelity with respect to both figure and finish as it is shown in Figure 3. The rms surface irregularity of the mirror is  $RMS_i = 4.78$  nm with a non-rotationally symmetric contribution of  $RMS_a = 1.31$  nm. The rms surface roughness is  $R_q = 0.13$  nm over a spatial frequency range of  $\nu \approx 0.4 \text{ mm}^{-1} \dots 100 \text{ mm}^{-1}$  which is relevant for small angle scattering around the specular direction. Wide angle scattering from the illumination mirror is blocked by an additional enclosure around the illumination module and by the relay optics in front of the detector, as will be explained later.

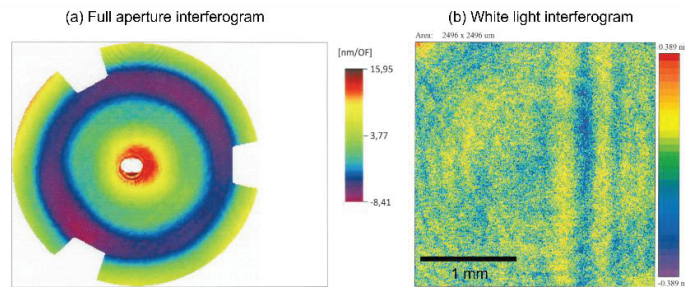


Figure 3: Figure and finish of the illumination mirror.

The matching optics with the source pinhole is mounted on a motorized focus stage that allows the adjustment of the source distance  $l_p$  from pinhole to mirror vertex within the range of  $l_p = 315 \text{ mm} \dots 455 \text{ mm}$ , corresponding to a shift of the pinhole image location from  $\infty$  to  $l_s - 200$  mm in front of the DUT. The adjustable focus is required to ensure a sharp image of the source pinhole at the location of the detector entrance aperture when samples with optical power (e.g. curved mirrors or gratings, lenses) are measured.

The DUT is mounted on a sample stage that is part of the instrument's axes assembly. The sample stage can accommodate samples up to  $200 \times 200 \times 200 \text{ mm}^3$  with a mass of up to 1 kg. It consists of a motorized rotation stage for the adjustment of the angle of incidence ( $\theta_y$ ,  $360^\circ$  continuous travel), three motorized linear stages for the sample positioning ( $x$ ,  $y$ , and  $z$ , each  $\pm 50 \text{ mm}$ ) and two manual goniometers with a common center of rotation 130 mm above the last stage for tilt ( $\theta_x$ ,  $\pm 10^\circ$ ) and roll adjustment ( $\theta_z$ ,  $\pm 8^\circ$ ). When the linear stages are centered, the common center of rotation of the goniometers is on the rotation axis of the  $\theta_y$  stage and coincides with origin of the instrument's coordinate system. The center of the illumination beam passes through the origin of this coordinate system.

The support of the sample stage is fed through the center of the motorized detector rotation stage, such that the  $\theta_y$  stage and the detector stage share a common rotation axis. The detector rotation stage carries a cantilever which holds the detector assembly. The distance from the center of the detector entrance aperture to the rotation axis is  $l_d = 350 \text{ mm}$ . The detector axis has a travel range from  $-95^\circ$  to  $275^\circ$ , which means that it covers a full circle of  $360^\circ$  but it cannot travel continuously.

Finally, the detector assembly is the core feature that distinguishes ELSA/CG-S from other instruments like CASI. It consists of a  $7.5 \times 7.5 \text{ mm}^2$  large laser-cut entrance aperture, a relay optics with a magnification of  $M = -0.38$ , and a camera with a back-illuminated silicon sCMOS sensor ( $2048 \times 2048$  pixels,  $6.5 \mu\text{m}$  pixel pitch). The purpose of these components will be explained in the next section. The detector assembly is mounted on a manual linear stage to align the  $y$  position of the entrance aperture with the instrument coordinate system. The camera and the relay optics are mounted on another horizontal linear stage for adjusting the focus of the entrance aperture image on the sCMOS camera chip.

## 2.2 Detector Design

As mentioned in the previous section, the source pinhole is not projected directly on the camera sensor but onto an entrance aperture which is in turn imaged onto the sensor by a relay optics. This intermediate step is a key feature of ELSA/CG-S that enables a good instrument signature with an imaging detector. The concept has already been used in a previous scatterometer for plane gratings described in [7].

In ELSA/CG-S the relay optics serves multiple purposes: Firstly, it protects the camera sensor from dust. The back-illuminated camera sensor has no cover glass and the camera is used without protective window to avoid stray light. Hence, the camera sensor is unprotected, and any dust or dirt would cause irreparable damage. The relay optics seals the camera and protects the sensor. When the relay optics has to be removed, the sensor is protected by a mechanical shutter.

Secondly, the relay optics adapts the camera pixel size to the actual resolution requirements. With a detector distance of  $l_d = 350 \text{ mm}$ , the camera sensors' physical pixel size of  $6.5 \mu\text{m}$  would correspond to an angular width of 3.83 arc seconds which is much smaller than the apparent angular width of the diffraction limited spot at  $\lambda = 633 \text{ nm}$  of about 53 arc seconds. The resulting oversampling would limit the achievable signal to noise ratio (SNR) unnecessarily. To avoid this, the physical pixels size is enlarged by the relay optics by a factor of 2.63. This results in a 6.92 times higher photon flux per pixel while readout noise and dark current noise are unaffected.

Thirdly, the relay optics restricts the field of view of the camera sensor. The relay optics contains an adjustable aperture stop. The stop position is chosen such that entrance pupil location of the relay optics coincides with the location of the DUT. The stop size is adjusted such that the entrance pupil diameter is about 2 to 3 times of the illuminated area on the DUT. Thus, only light scattered from the illuminated area of the sample can reach the camera sensor while stray light, e.g. light scattered from the walls of the enclosure, and wide angle scattering from the illumination mirror is blocked. This is similar to the function of the field lens in front of the detector of the CASI scatterometer.

Fourthly, the relay optics blocks light from parts of the camera sensor. The demagnified image of the entrance aperture covers only the central region of about  $440 \times 440$  pixels on the camera sensor. The dark regions of the camera sensor are used for dark count estimation and background correction during the image acquisition. This allows to account for a drift of the sensor temperature and an uneven temperature distribution across the camera sensor.

And finally, the sharp image of the entrance aperture edges in the sensor plane allows imaging the low intensity wings of sharp features while the high intensity central region is blocked. This enhances the dynamic range of the detector and allows an improvement of the small angle signature by a procedure that we call peak bracketing. When a high intensity feature is imaged onto the camera sensor, the dynamic range that can be achieved by collecting an HDR image series at various exposure values is limited by the product of the sensor's dynamic range and the blooming factor. This product is about  $10^7$  to  $10^8$  for the camera used in ELSA/CG-S. Also, when a high intensity feature enters the relay optics, its lenses cause scattering and ghosting. In combination with scattering from the camera sensor, this creates a background

illumination level, that limits the dynamic range and lifts the level of the small angle signature. To prevent these effects, only the high intensity part of an image is used when a sharp feature is detected on the sensor. The low intensity wings of the feature are then recorded in additional passes where the high intensity region is blocked by the entrance aperture. An example of this procedure is shown in section 3.1.

### 2.3 Noise Estimation and Minimum Detectable BSDF

A very important parameter of a scatterometer is the minimum detectable BSDF. In the following, we will estimate this value for the detection scheme that is implemented in ELSA/CG-S.

From Equation (2), the scattered power that is received by a sensor pixel is

$$\Delta P_s = P_{in} \cdot \text{BSDF} \cdot \cos(\theta_s) \cdot \Delta\Omega. \quad (3)$$

This can be converted into the number of electrons per pixel that is collected within the maximum integration time  $\tau_{max}$  of the camera:

$$N_e = \frac{\eta \Delta P_s \tau_{max}}{E_{phot}}. \quad (4)$$

Thereby  $\eta$  is the sensor quantum efficiency and  $E_{phot}$  is the photon energy. As the number of photons that is received within a given time interval follows a Poisson distribution, the associated variance of the collected photo electrons is:

$$\sigma_e^2 = N_e \quad (5)$$

During image acquisition, the dark count per pixel is estimated from the average dark count of an unilluminated region of the sensor. For each pixel, the average of  $N_d$  dark pixels is taken into account. While this corrects the average offset, it cannot correct for the shot noise, as the thermal electrons also follow a Poisson distribution that gives rise to the following dark count variance:

$$\sigma_d^2 = R_d \tau_{max} \cdot \left(1 + \frac{1}{N_d}\right). \quad (6)$$

The sampling of the collected electrons by the sensor electronics is subject to additional readout noise with variance  $\sigma_{ro}^2$ . The variance per pixel is the sum of all individual variance contributions. When the signal is calculated as the average of  $N_{avg}$  pixels, the total variance is given by:

$$\sigma^2 = \frac{\sigma_e^2 + \sigma_d^2 + \sigma_{ro}^2}{N_{avg}}. \quad (7)$$

Dividing the number of collected electrons by the square root of the variance yields the signal to noise ratio:

$$\text{SNR} = \frac{N_e}{\sigma} \quad (8)$$

Solving Equation (8) for  $N_e$  yields the minimum number of photo electrons that have to be collected to reach a desired SNR:

$$N_{min} = \frac{\text{SNR}^2}{2N_{avg}} + \text{SNR} \sqrt{\frac{\text{SNR}^2}{4N_{avg}^2} + \frac{\sigma_d^2 + \sigma_{ro}^2}{N_{avg}}} \quad (9)$$

Finally, inserting  $N_{min}$  in Equation (4) yields the minimum detectable BSDF with a given target SNR at a given input power  $P_{in}$ :

$$\text{BSDF}_{min} = \frac{N_{min} E_{phot}}{P_{in} \Delta\Omega \cos \theta_s \eta \tau_{max}} = \frac{E_{phot}}{P_{in} \Delta\Omega \cos \theta_s \eta \tau_{max}} \left( \frac{\text{SNR}^2}{2N_{avg}} + \text{SNR} \sqrt{\frac{\text{SNR}^2}{4N_{avg}^2} + \frac{\sigma_d^2 + \sigma_{ro}^2}{N_{avg}}} \right). \quad (10)$$

Using the parameters from Table 2, the minimum detectable BSDF has been calculated for various values of SNR and  $N_{avg}$ . The results are shown in Table 3Table 1. From this table it is apparent that the minimum BSDF that can be detected by a single pixel is limited. However, low BSDF levels are usually not associated with sharp features but broad scattering.

In this case, the minimum detectable BSDF can be easily improved by averaging a certain number of pixels. For example, averaging  $N_{avg} = 256$  pixels corresponds to a  $16 \times 16$  pixel region with an angular extent of  $0.045^\circ$ .

The strength of ELSA/CG-S' detection scheme is, that the decision about the averaging can be deferred to the postprocessing of the acquired data and adaptive methods can be applied: Sharp BSDF features can be detected at the single pixel level while in featureless regions, where high angular resolution is not as important, the average over a larger number of pixels can be calculated to improve the SNR. As all measurement data is stored with the full pixel resolution, the postprocessing scheme can be changed at any later time without the need to acquire new measurements.

Table 2: Parameters used for the noise estimation.

Input power $P_{in}$	3.5 mW
Quantum efficiency $\eta$	0.85
Photon energy $E_{phot}$	$3.130 \cdot 10^{-19}$ J
Pixel solid angle $\Delta\Omega$	$2.338 \cdot 10^{-9}$ sr
Dark count rate $R_d$	$42 \text{ s}^{-1}$
Maximum integration time $\tau_{max}$	0.5 s
RMS readout noise $\sigma_{ro}$	1.9
No. of pixels for dark count estimation $N_d$	400
Scatter angle $\theta_s$	$60^\circ$

Table 3: Minimum detectable BSDF for various numbers of pixel averages and target SNRs.

	$N_{avg} = 1$	$N_{avg} = 16$	$N_{avg} = 256$
SNR = 1	$9.71 \cdot 10^{-7} \text{ sr}^{-1}$	$2.25 \cdot 10^{-7} \text{ sr}^{-1}$	$5.52 \cdot 10^{-8} \text{ sr}^{-1}$
SNR = 3	$3.55 \cdot 10^{-6} \text{ sr}^{-1}$	$7.10 \cdot 10^{-7} \text{ sr}^{-1}$	$1.68 \cdot 10^{-7} \text{ sr}^{-1}$
SNR = 10	$2.13 \cdot 10^{-5} \text{ sr}^{-1}$	$2.82 \cdot 10^{-6} \text{ sr}^{-1}$	$5.84 \cdot 10^{-7} \text{ sr}^{-1}$

## 2.4 Data Acquisition Procedure

Before we discuss measurements obtained with ELSA/CG-S, we will briefly describe the data acquisition procedure of the instrument, as it differs from a single channel measurement.

An ELSA/CG-S measurement corresponds to a scan of the detector angle from a given start angle to a given end angle with a constant angle step. At each detector position a high dynamic range (HDR) image with an angular FoV of about  $1.23^\circ \times 1.23^\circ$  is acquired. When the peak bracketing procedure described in section 2.2 is enabled, the centroid, the relative power, and the width of the strongest feature in each HDR image is calculated. For each feature that qualifies for bracketing, two additional HDR images are queued for acquisition at the end of the main scan. The region that is covered by these additional bracketing images (excluding a small overlap region) is marked as invalid in the main scan data.

After all images have been acquired, the individual HDR images are blended into a single large HDR image. A linear interpolation kernel is used for the blending procedure. Overlapping regions of HDR images are averaged. To ensure a proper peak detection, an overlap of 20% to 30% between adjacent HDR images is required, depending on the maximum peak width that shall be considered for bracketing. This requirement results in a typical detector step size of about  $1^\circ$ , i.e. for a scan from  $-15^\circ$  to  $15^\circ$  about 31 HDR images plus additional bracketing images are acquired. As the acquisition of a single HDR image takes about 10 seconds, scan times are quite fast even for a large angular range. Multiple sample configurations (i.e. sample positions or incidence angles), and detector scan centers can be queued for automated batch measurements.

Individual HDR images are acquired by capturing a series of images with increasing effective exposure time  $\tau_{\text{eff}} = \tau T_{\text{filter}}$ , where  $\tau$  is the actual exposure time and  $T_{\text{filter}}$  is the transmittance of the currently selected neutral density filter. The maximum effective exposure time is limited to  $\tau_{\text{eff}} \leq \max(\tau_{\text{eff,valid}}) \cdot f_{\text{blooming}}$  where  $\max(\tau_{\text{eff,valid}})$  is the largest effective exposure time that did not cause saturation (i.e. a count value exceeding 80% of the maximum count value) on any pixel, and  $f_{\text{blooming}}$  is the maximum overexposure factor that will not cause blooming. At each  $\tau_{\text{eff}}$ , all pixels that are not saturated are normalized to  $\tau_{\text{eff}}$  and copied to the final HDR image, replacing any existing data obtained with lower  $\tau_{\text{eff}}$ , while all saturated pixels are discarded.

### 3 MEASUREMENTS

After having discussed the design and the measurement procedures of ELSA/CG-S, we will now present some measurements that illustrate the real-life performance of the instrument. First, we will show measurements of the instrument signature and measurements from a diffuse Spectralon® reflectance standard, that demonstrate the absolute calibration accuracy. After that, we will present measurements of plane and curved diffraction gratings with high groove-densities that illustrate the benefits of the imaging detector. For comparison, similar measurements of the same samples obtained with a CASI scatterometer will be shown as well.

#### 3.1 Instrument Signature and Absolute Calibration Accuracy

Figure 4 shows three different measurements of the ELSA/CG-S signature (blue, orange, and green curves) along with a signature measurement from CASI in its nominal configuration ( $l_d = 480$  mm, red curve). The blue and the orange curves depict the ELSA/CG-S signature in the current instrument configuration. The blue curve was obtained without peak bracketing, the orange curve was measured with peak bracketing enabled. The green curve corresponds to the signature of the instrument with active peak bracketing in an earlier instrument configuration.

The blue signature curve without peak bracketing clearly demonstrates the deteriorating effects described in section 2.2: The signature level is elevated, and large jumps are visible at about  $\pm 0.6^\circ$ , which corresponds to the FoV of the central HDR image where the specular beam hits the relay optics and the camera sensor. When peak bracketing is enabled, the steps disappear and the signature level close to the specular peak is significantly decreased. Figure 5 shows regions in the vicinity of the specular peak of the two-dimensional HDR data that the blue and the orange curve were derived from: Figure 5(a) corresponds to the signature measurement without peak bracketing. The blue curve of Figure 4 was extracted from this by averaging the image rows between the two white horizontal lines. In this image, the specular peak is surrounded by ring-like diffraction patterns that are caused by the lenses of the relay optics and reflections from the camera sensor. Additionally, the background level within the region of the central HDR image is clearly elevated. Figure 5(b) shows an intermediate result of the measurement with activated peak bracketing, where the regions adjacent to the specular peak have been invalidated. The regions were filled with data from additional measurements that are shown in Figure 5(c). For the acquisition of these images, the high intensity region of the peak was moved just onto the entrance aperture of the detector and did not enter the relay optics. Consequently, the fringes and the elevated background level are gone. Figure 5(d) shows the result after blending all HDR images. It is free of artifacts except from a thin bright vertical stripe close to the peak. This stripe cannot be removed as ELSA/CG-S does not have a motorized vertical detector axis, and hence is not capable of vertical peak bracketing. The remaining eye shaped structure around the specular peak is a true signature feature. The orange curve of Figure 4 has been extracted from this image.

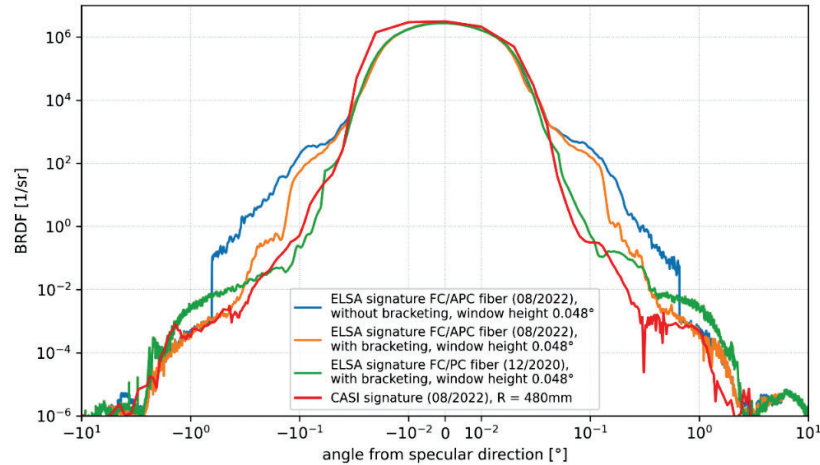


Figure 4: Signatures of ELSA/CG-S and CASI. The meaning of the various ELSA/CG-S signature curves is explained in the text.

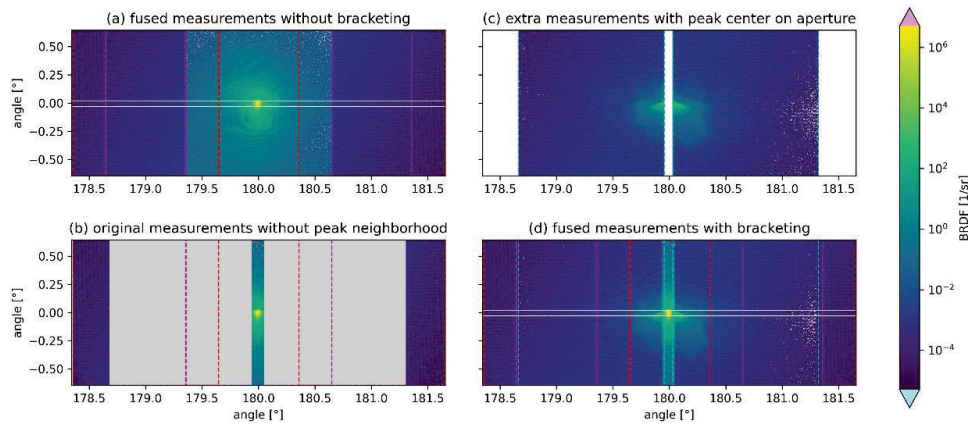


Figure 5: Working principle and effect of the peak bracketing procedure. The gray areas in (b) indicate invalidated values that are replaced with data from additional bracketing measurements shown in (c). The colored dashed boxes indicate the ROIs of the individual measurements. The white horizontal lines indicate the averaging window of the line plots shown in Figure 4.

A comparison between the orange ELSA/CG-S signature with the red CASI signature reveals, that ELSA/CG-S is close to the signature of CASI except for the shoulders around  $\pm 0.1^\circ$  that are caused by the eye shaped feature mentioned above. The green signature measurement obtained with an earlier configuration of ELSA/CG-S does not suffer from this feature and matches the CASI signature in this region. The slightly higher shoulders around  $\pm 1^\circ$  in this measurement are most likely due to a too large setting of the relay optics aperture stop.

The difference between ELSA/CG-S signatures in the earlier configuration and the current configuration has most likely been caused by a realignment of the matching optics after the replacement of the fiber between attenuation module and illumination module. We are very confident that the original signature performance can be restored with some minor changes. Unfortunately, it was not possible to apply these changes in time for the grating measurements that are shown below.

Both ELSA/CG-S and CASI measure the absolute BSDF: The input laser power is measured before a scan (in case of ELSA/CG-S) or tracked during a scan (in case of CASI) and the detector solid angle, the detector gain, and the detector responsivity are calibrated for the specific detector distance and measurement wavelength. Hence, the detector readings of both instruments can be converted directly into BSDF values and no reference measurement is required.

The absolute calibration accuracy of both scatterometers was assessed by measuring the BRDF of a diffuse Spectralon® reflectance standard. The results of these measurements are shown in Figure 6(a). For ELSA/CG-S three different post processing methods were applied: Averaging of the two-dimensional data over the full vertical height of the detector FoV (blue), filtering with a two-dimensional Gaussian filter with a standard deviation of  $\sigma = 0.15^\circ$  (cyan), and averaging over a circular region at discrete angular positions that correspond to the CASI scan steps and aperture sizes (dark yellow). The last method simulates the single channel data acquisition of the CASI scatterometer. From CASI two measurements are shown: A measurement in the nominal configuration with a detector distance of  $l_d = 480$  mm (magenta) for which the instrument has been calibrated, and a measurement with a shorter detector distance of  $l_d = 355$  mm (red), which had to be used for one of the grating measurements presented below.

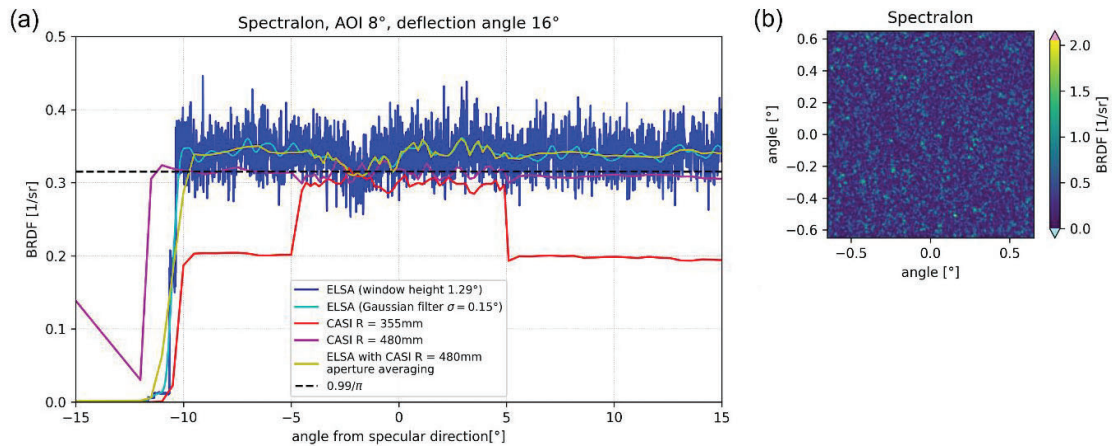


Figure 6: (a) Comparison of the Spectralon® measurements from ELSA/CG-S and CASI. (b) ELSA/CG-S detector image of the speckle pattern that is created by the sample.

The blue curve from ELSA/CG-S appears to be very noisy. This effect is due to fast angular variation of the speckle pattern shown in Figure 6(b), which results from the coherent illumination of the diffusely scattering sample with a limited beam footprint (diameter ca. 3 mm). Averaging of the two-dimensional data only along the vertical direction is not sufficient, but both of the applied 2D averaging methods reduce the signal variation to the same level as observed on the CASI scatterometer.

Both the measurements from ELSA/CG-S and the measurements from CASI at  $l_d = 480$  mm are very flat as expected from a Lambertian scatterer. While the CASI measurement is right on the expected level indicated by the black dashed line, the ELSA/CG-S measurement is slightly too high (less than 8%). We suspect a combination of two effects to be responsible for this error. Firstly, the calibration of the sensor quantum efficiency might have been slightly off. Unfortunately, we did not check this before the measurement. Secondly, ELSA/CG-S does not monitor the laser power during the measurement, as this is difficult to implement with the chosen attenuator design. The power level of ELSA/CG-S is sufficiently stable on the time scale of a measurement that the lack of a live power monitoring does not cause accuracy issues as long as the power is measured regularly before and between measurements to compensate for any long-term power drift. The power measurement used for the presented Spectralon measurement was about 30 to 60 minutes old, so some slight power drift might have occurred. To avoid this source of error in future, a warning or even an automated power measurement sequence could be implemented in the control software.

The measurement obtained with CASI at a shorter detector distance of  $l_d = 355$  mm is very close to the measurement at  $l_d = 480$  mm for scatter angles up to  $\pm 5^\circ$  from the specular direction. However, when the instrument changes to the largest aperture size, the measured BRDF drops abruptly, and the absolute error is about 30%. This illustrates, that care has to be taken when the instrument configuration is changed as this might invalidate the calibration.

### 3.2 Diffraction Gratings

We measured 3 different diffraction gratings both on ELSA/CG-S and on CASI: a plane replica of a mechanically ruled grating, a plane holographic master grating and a curved replica of a holographic Rowland circle grating. The relevant parameters of the gratings are summarized in Table 4.

Table 4: Parameters of the investigated gratings.

	Plane Ruled	Plane Holographic	Concave Holographic
Zeiss no.	263232-xx12-424	263232-xx92-824	792029-0000-000
Line density	1200 mm <sup>-1</sup>	1200 mm <sup>-1</sup>	1500 mm <sup>-1</sup>
Radius of curvature	∞	∞	749.9 mm
Grating technology	mechanically ruled	holographic	holographic
Groove profile	blazed	blazed	sine
Nominal blaze wavelength at 4° CAD	300 nm	230 nm	-
Grating type	replica	master grating	replica
AOI at 20° deflection angle	32.7°	32.7°	38.8°
Measured efficiency in test configuration (ELSA/CG-S, TM)	42%	21%	51%

Scattering from all gratings was measured around the -1<sup>st</sup> diffraction order which is diffracted back towards the incident beam. The deflection angle between incident beam and -1<sup>st</sup> order was set to 20°. The position of the source pinhole was adjusted for the minimum radial spot size (i.e. the best focus). It would have been possible to measure specifically in the tangential or the sagittal focus on ELSA/CG-S, as the two-dimensional spot image can be used for an easy alignment, but this possibility was not used because we focused on comparability of the measurement between CASI and ELSA/CG-S.

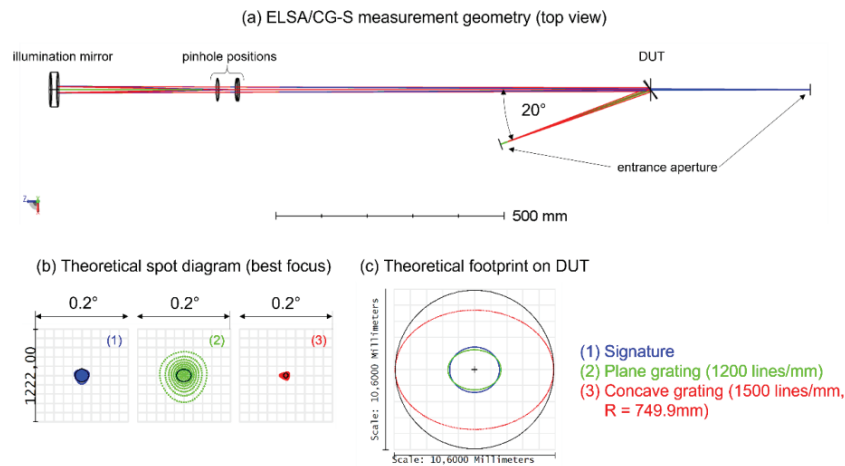


Figure 7: Measurement geometry and theoretical spot parameters on the ELSA/CG-S scatterometer.

Both, for the grating samples and the signature configuration we modeled the measurement geometry with Zemax. The results for ELSA/CG-S are shown in Figure 7 and the results for CASI are shown in Figure 8. The spot sizes and the beam footprints are very similar between the two instruments. However, in order to measure the curved grating with CASI, the

detector distance had to be reduced to  $l_d = 355$  mm. At CASI's nominal detector distance of  $l_d = 480$  mm it was not possible to obtain a reasonable focus spot. Please note that the curved grating has a smaller theoretical spot size than the signature configuration and exhibits a substantially larger beam footprint on the grating. This is due to the large defocus of illumination beam that is required to compensate for the optical power of the curved grating. The plane gratings on the other hand have a significantly worse spot size than the signature while the beam footprint at the grating location is comparable to the signature configuration. The nominal spot size of the plane gratings is about 30% better in the CASI geometry than in the ELSA/CG-S geometry.

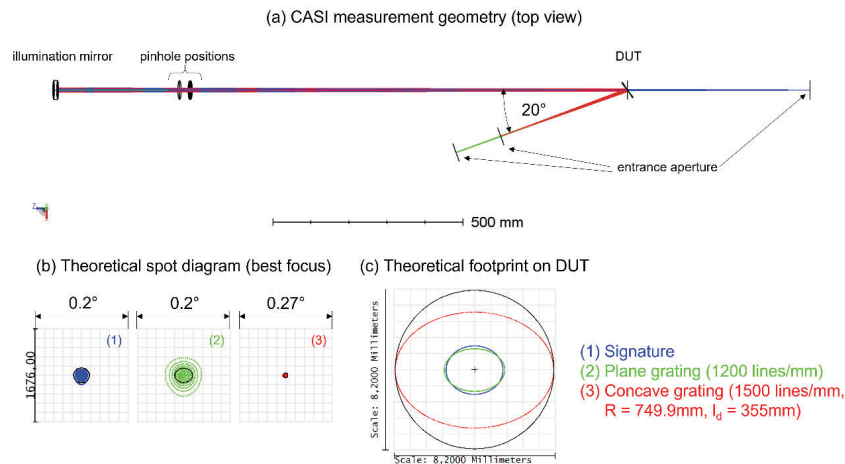


Figure 8: Measurement geometry and theoretical spot parameters on the CASI scatterometer.

The results of the plane holographic grating are shown in Figure 9. Again, three different post processing methods were applied to the two-dimensional ELSA/CG-S data: Vertical averaging over a band of  $0.048^\circ$  (17 pixels) around the center of the diffraction peak (blue), two-dimensional Gaussian filtering with  $\sigma = 0.028^\circ$  (cyan), and averaging over variable circular regions according to CASI's aperture sizes and aperture switching angles (dark yellow). As discussed above, the two-dimensional filtering suffers less from speckle artifacts than the vertical averaging. However, the chosen Gaussian filter already broadens the width of the diffraction peak and thus limits the resolution at small angles. The CASI measurements are shown in red. The instrument signatures without sample are shown as dashed lines.

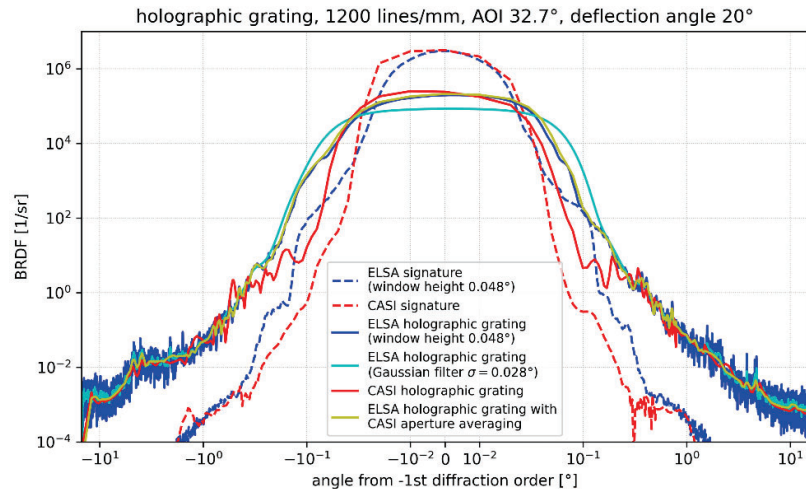


Figure 9: Comparison of the plane holographic grating measurements.

Outside a region of  $\pm 0.25^\circ$  from the diffraction peak, the measurements from ELSA/CG-S and CASI agree very well. At smaller angles, the CASI measurement indicates a narrower width of the diffraction peak which is consistent with the smaller nominal spot size of the plane gratings for the CASI geometry. Also, ELSA's eye-shaped signature artifact, that has been discussed above, might contribute to the shoulders around  $\pm 0.1^\circ$ . The grating has multiple very weak rings. In the vertically averaged ELSA/CG-S data (blue curve) these rings can be seen for example at  $\pm 3.8^\circ$  and at  $\pm 4.7^\circ$ . In the Gaussian filtered data and especially in the CASI measurements, these features are underestimated.

The results for the plane ruled grating are shown in Figure 10. The appearance of the diffraction peak is very similar to the results from the plane holographic grating. At angles farther than  $\pm 1^\circ$  away from the diffraction peak, there is a significant difference between the ELSA/CG-S and the CASI measurements. While the ELSA/CG-S measurement approaches a constant scatter level, the CASI measurement shows a step-like decay of the BRDF. The steps occur at the angles where the CASI scatterometer switches the detector apertures during the measurement. When the ELSA/CG-S measurement is post-processed with a CASI-like aperture averaging, the steps are reproduced. This clearly shows that steps are not real BRDF features but artifacts from the way how a CASI measurement is performed. Figure 12(a) shows an image of the two-dimension ELSA/CG-S data in the vicinity of the diffraction peak. The CASI aperture sizes at the switching positions are overlaid as white circles on this image. The image shows, that the grating BRDF exhibits a very narrow stripe-like feature along the grating's dispersion direction. This is a typical feature of ruled gratings and originates from random step errors of the ruling machine [8]. The extent of this feature along the cross-dispersion direction is of the same order as the extent of the diffraction peak. Only when the detector aperture is smaller than the height of the stripe, a CASI measurement will produce accurate results. When the aperture height exceeds the height of the stripe, the stripe magnitude will be underestimated, as the average between the stripe and the regions with much lower scattering above and below will be measured. The larger the aperture gets, the less the stripe contributes to the overall signal.

On top of the stripe, the grating has a ghost at about  $14.5^\circ$  (at the very edge of the plot). This ghost is resolved by the high-resolution ELSA/CG-S data but not in the CASI measurement, due to the large aperture setting at this angle. It is only recognizable by a small upwards step in the CASI data and in the ELSA/CG-S data with CASI-like aperture averaging.

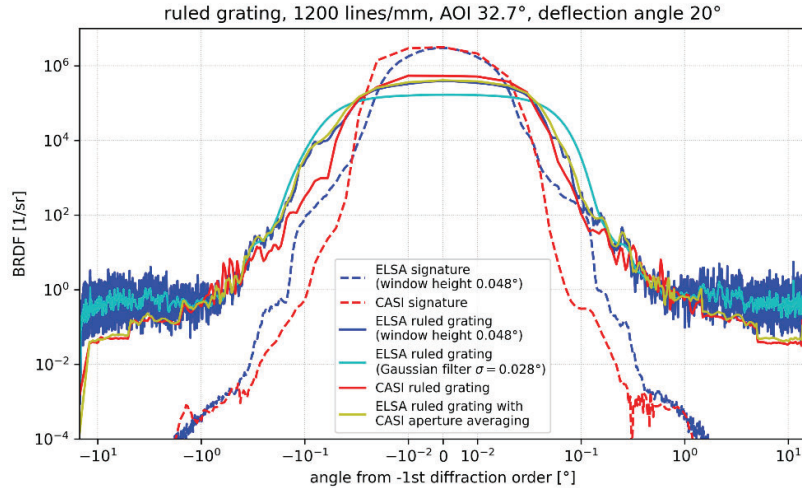


Figure 10: Comparison of the ruled grating measurements.

The results of the measurements of the concave holographic grating are shown in Figure 11(a). The grating has been measured on CASI with a reduced detector distance that does not correspond to the calibration configuration of the instrument. Data obtained from the ELSA/CG-S measurement with different post-processing methods is shown in blue, cyan, and dark yellow. Additionally, an ELSA/CG-S measurement without peak bracketing is shown in green. The original CASI measurement is shown in red, data from the CASI measurement that have been corrected for the calibration error that can be seen in Figure 6, are shown in magenta. As with the plane holographic grating, the ELSA/CG-S data and the corrected CASI data are in very good agreement at angles farther than  $\pm 0.25^\circ$  away from the diffraction peak. This time, the diffraction peak is resolved better by ELSA/CG-S at very small angles. As indicated by the Zemax calculation, the spot size with the curved grating is indeed better than the signature spot size without sample. Around  $0.1^\circ$ , the ELSA/CG-S measurement exhibits shoulders that exceed the CASI measurement. We don't think that this is purely related to the eye-shaped signature feature of ELSA/CG-S discussed above for this specific grating. A close-up image of the diffraction peak shown in Figure 11(b) reveals an elongated feature along the grating's dispersion direction with very narrow extent along the cross-dispersion direction. We suspect that this feature might be due to amplified spontaneous emission from the laser that is spread out by the high grating dispersion.

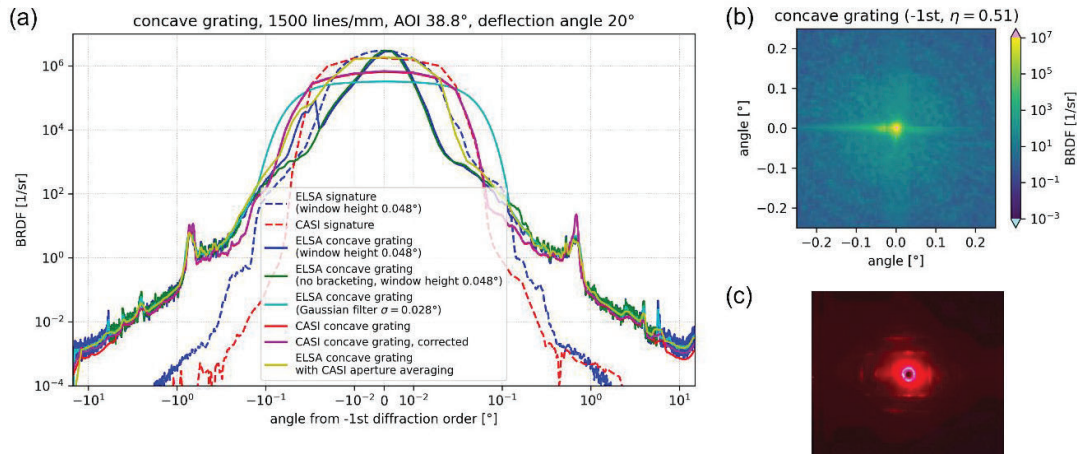


Figure 11: (a) Comparison of the concave holographic grating measurements. (b) Close-up image of the 2D ELSA/CG-S data around diffraction peak. (c) Overexposed photograph of the grating's ring and bar-like features.

The ELSA/CG-S measurement with activated peak bracketing exhibits a step like artifact very close to the diffraction peak that disappears when the peak bracketing is disabled. This artifact seems to be a stitching error due to a misalignment of  $0.014^\circ$  between the peak image and the bracketing images. The misalignment might be caused by backlash of the detector stage as the detector moves opposite to the original scan direction when it returns for the acquisition of the bracketing images. It should be possible, to avoid such artifacts by adapting the control software.

The curved holographic grating exhibits a prominent ring at about  $0.7^\circ$  and weak additional ring and bar-like features farther way from the diffraction peak. The innermost ring is resolved equally well by ELSA/CG-S and by CASI. The other structures, however, are underestimated by the CASI measurement because they are sampled with a large aperture. This is illustrated in Figure 12(b).

The ring and bar-like features can be seen with the naked eye or on an overexposed photograph of a white screen as shown in Figure 11(c). Such a simple investigation easily allows to plan additional CASI measurements with adjusted aperture settings to resolve these features. Of course, this still costs additional time and effort compared to a single ELSA/CG-S measurement.

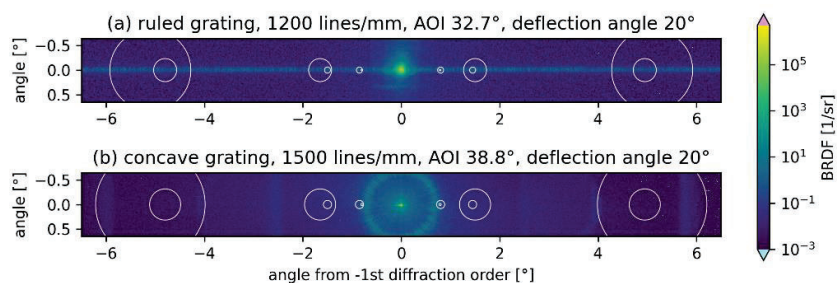


Figure 12: Images of the 2D ELISA/CG-S data of the ruled grating (a) and the curved holographic grating (b). White circles indicate the extent of the detector apertures of the equivalent CASI measurement before and after aperture switching.

#### 4 CONCLUSION AND SUMMARY

We have presented the design and implementation of a new high resolution scatterometer, ELSA/CG-S, that utilizes an imaging sCMOS sensor instead of a conventional single channel detector, and we have explained the rationale behind some of the design choices that have been made. We have demonstrated that these choices in conjunction with an appropriate measurement strategy allow to achieve a signature performance and sensitivity that is competitive in comparison to current commercially available state of the art instruments.

Furthermore, we have illustrated the real-live performance of the instrument with measurements of the scattering from high groove-density diffraction gratings and validated the results against measurements performed with ESTEC's commercial CASI scatterometer. These measurements generally show a very good agreement between the two instruments. Minor deviations have been discussed and explained.

With the grating measurements, we have also demonstrated the flexibility that is provided by ELSA/CG-S' high detector resolution. No planning of any detector aperture settings before a measurement or multiple measurements with different aperture settings are required to ensure the accurate detection and characterization of localized features like ghosts, stripes, or rings. Each measurement with ELSA/CG-S is performed at the full sensor resolution throughout the complete angular range of the measurement and the access to the 2D sensor data allows an easy identification of relevant BSDF features even far away from the scan center. For further analysis, e.g. the extraction of BSDF cross-sections, the choice between high angular resolution and low noise level has to be made only after the measurement by selecting an appropriate post-processing method. Multiple post-processing methods can be applied to the same measurement as needed.

This flexibility comes at no cost with respect to the measurement time. The large FoV covered by the entrance aperture allows measuring with a large angular step of about  $1^\circ$ . In combination with the fast acquisition time for a single HDR image, this results in very fast measurement times in the order of 5 minutes for a scan from  $-15^\circ$  to  $15^\circ$  around an angle of interest.

## REFERENCES

- [1] Tomuta, D., Kirschner, V., Taccola, M., Miranda, M., Arts, M., “Straylight measurements on gratings: challenges and limitations”, Proc. SPIE 11180, 111804P (2019).
- [2] Kroneberger, M., Tomuta, D., Mezger, A., “Straylight of curved gratings: an interlaboratory comparison”, Proc. SPIE 11180, 111808C (2019).
- [3] Nicodemus, E., “Reflectance nomenclature and directional reflectance and emissivity,” Appl. Opt. 9, 1474–1475 (1970).
- [4] Stover, J. C., “Optical scattering: measurement and analysis”, 3rd ed., SPIE optical engineering press, Bellingham, Washington, (2012).
- [5] CASI Data Sheet, The Scatter Works Inc., <https://thescatterworks.com/wp-content/uploads/CASI-Data.pdf> (accessed on August 29th, 2022).
- [6] ALBATROSS-TT Table-Top System for Light Scatter Measurements, Fraunhofer Institute for Applied Optics and Precision Engineering, <https://www.iof.fraunhofer.de/content/dam/iof/en/documents/pb/en-Table-Top-Streulichtmesssystem-Albatross-TT.pdf> (accessed on August 29th, 2022).
- [7] Koch, F., Zilk, M., Schnabel, M., Glaser, T., “High-resolution Czerny-Turner scatterometer for BRDF measurements”, Proc. SPIE 11056, 110561C (2019).
- [8] Koch, F., Zilk, M., Glaser, T., “Semi-analytic modeling of diffraction grating BRDF using scalar Fourier optics“, Proc. SPIE 11783, 1178304 (2021).